Theoretical Studies of Non Inductive Current Drive in Compact Toroids

R. Farengo, A.F. Lifschitz, K.I. Caputi, N.R. Arista,
Centro Atomico Bariloche and Instituto Balseiro
S. C. de Bariloche, RN, Argentina

and R.A. Clemente
Instituto de Física Gleb Wataghin
Universidade Estadual de Campinas
Campinas, SP, Brasil

Received on 26 June, 2001

Three non inductive current drive methods that can be applied to compact toroids are studied. The use of neutral beams to drive current in field reversed configurations and spheromaks is studied using a Monte Carlo code that includes a complete ionization package and follows the exact particle orbits in a self-consistent equilibrium calculated including the beam and plasma currents. Rotating magnetic fields are investigated as a current drive method for spherical tokamaks by employing a two dimensional model with fixed ions and massless electrons. The time evolution of the axial components of the magnetic field and vector potential is obtained by combining an Ohm's law that includes the Hall term with Maxwell's equations. The use of helicity injection to sustain a flux core spheromak is studied using the principle of minimum rate of energy dissipation. The Euler-Lagrange equations obtained using helicity balance as a constraint are solved to determine the current and magnetic field profiles of the relaxed states.

I Neutral beam current drive

The use of neutral beams to sustain the current in a field reversed configuration (FRC) reactor was proposed many years ago [1]. More recently, laboratory experiments where a neutral beam is injected into an existing FRC have been performed [2]. Unfortunately, the lifetime of these experiments is much shorter than the slowing down and thermalization times and therefore our results, which apply to a steady-state situation, can not yet be compared with the experimental observations. Spheromaks are formed and sustained by helicity injection and the use of alternative methods is generally not considered. However, using neutral beams to produce part of the current could reduce the amplitude of the fluctuations required for helicity injection current drive thus improving the confinement. This behavior has been observed in recent RFP experiments [3]. In addition, the use of neutral beams will result in additional heating and better control of the current profile.

I.1 Monte Carlo code and equilibrium

The Monte Carlo code employed in this study follows the trajectories of an ensemble of beam particles moving in a self-consistent MHD equilibrium. The exact orbits are needed because the large radial excursions of the energetic beam particles prevent the use of gyro-averaging. Neutral particles are injected and the code calculates their ionization, stopping and thermalization. This information is used to reconstruct the spatial distribution of the beam density, current and transferred power and force in steady state.

The ionization processes included are ionization by Coulomb collisions with ions and electrons, ionization by charge exchange and multistep processes: i.e., excitation followed by ionization. The effect of Coulomb collisions is described using a Fokker-Plank collision operator and the momentum and energy transferred to electrons and ions are evaluated separately. The injection geometry is shown in Fig. 1. The beam is injected at the midplane ($z = 0$) and perpendicular to the mag-

netic axis. It is assumed to be cold and non divergent and is considered to be a point source (negligible cross section). Setting the values of the neutral injection current (I_N), the energy of the beam particles (E_N) and the impact parameter (b), the beam is completely determined.

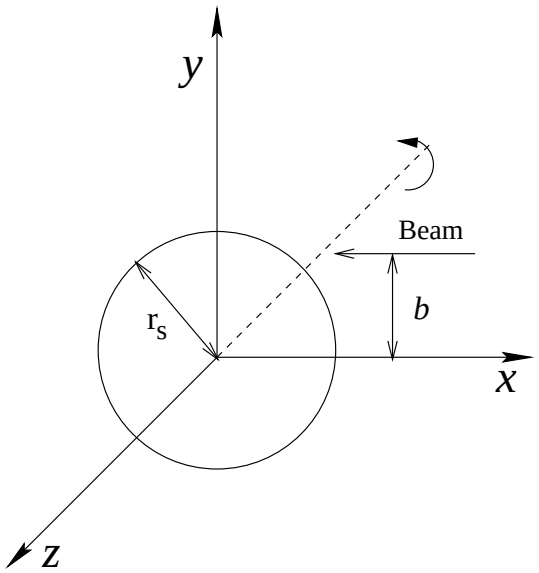

Figure 1. Injection geometry.

The plasma equilibria are solutions of the Grad-Shafranov equation with an extra term representing the beam current density. We assume that the beam pressure is small compared to the plasma pressure and therefore neglect the beam contribution to the pressure. The temperature is considered uniform and equal to 500 eV for both electrons and ions. With these approximations, the Grad-Shafranov equation can be written as:

$$r\frac{\partial}{\partial r}\frac{1}{r}\frac{\partial \psi}{\partial r}+\frac{\partial^2 \psi}{\partial z^2} = -16\pi^3 r^2 \frac{dP}{d\psi} - \frac{8\pi^2}{c^2}\frac{dI^2}{d\psi} - \frac{8\pi^2 r}{c} j_b \quad (1)$$

where ψ is the poloidal flux function, I is the poloidal current (set to zero for FRCs), j_b is the beam current density and P is the plasma pressure. We assume that the pressure and poloidal current are related to the poloidal flux though:

$$P(\psi) = G_0 \left[\frac{\psi}{\psi_0} - \frac{D}{2}\left(\frac{\psi}{\psi_0}\right)^2\right] \quad I^2(\psi) = I_0^2 \left(\frac{\psi}{\psi_0}\right)^2 \quad (2)$$

where G_0 and I_0 are constants, ψ_0 is the magnetic flux at the magnetic axis and D is the hollowness parameter. The equation is first solved with $j_b = 0$ and G_0 is determined by requesting that $B_z(r_s, 0) = B_0$. This equilibrium is employed to calculate the number of plasma particles. Then, we run the Monte Carlo code with this equilibrium and calculate j_b. Introducing j_b into eq.(1) a new equilibrium is calculated. This procedure is repeated until the solutions converge.

I.2 Ionization and trapping

In the code, a particle is considered lost when it reaches the ends of the plasma or when its radius becomes larger than the wall radius. For the FRC parameters considered in this study, the fraction of neutral particles that is not ionized is negligible small. For injection energies below 40 keV, the losses are significant only for $b \gtrsim 27cm$. As E_N increases, the maximum impact parameter which results in complete ionization becomes smaller. The particles reach the high density region even when ionization occurs far from there; all the particles injected with b between 15 and 25 cm cross the null. This is seen in Fig. 2 which shows the spatial distribution of beam ions after completing their first orbit. It is clear that there are significant differences with respect to devices with a large toroidal field, where the beam energy and the injection geometry are selected in order to trap the beam close to the plasma core.

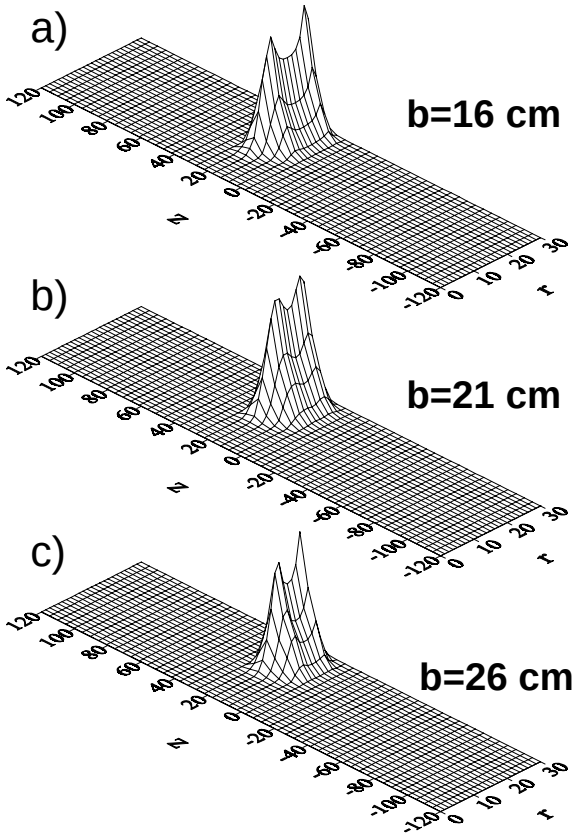

Figure 2. FRC, spatial distribution of beam ions after first orbit.

The situation in spheromaks is different due to the presence of a toroidal field and a close fitting flux conserver. Particles ionized inside the separattrix can nevertheless hit the wall due to their large Larmor radius. In addition, the toroidal field produces a fundamental change in the behavior of the particles. This can be seen comparing Fig. 3, with Fig. 2. For b smaller than the radius of the magnetic axis (32 cm) ionization can occur over a wide region and this results in a broad initial particle distribution. When $b = 32\ cm$, most particles are ionized and trapped close to the magnetic axis. Finally, when $b > 32\ cm$ the particles are trapped in orbits that oscillate around a given flux surface. The amplitude of this oscillation depends on the injection energy. Another consequence of the presence of a toroidal field is that a fraction of the particles, which depends on the injection energy and b, becomes trapped in banana type orbits. This is shown in Fig. 4, which presents a plot of lost and trapped particles as a function of the injection energy for three values of b. At low injection energy, a large fraction of the particles become trapped in banana orbits while at high energy the dominant effect is particle losses due to collisions with the wall.

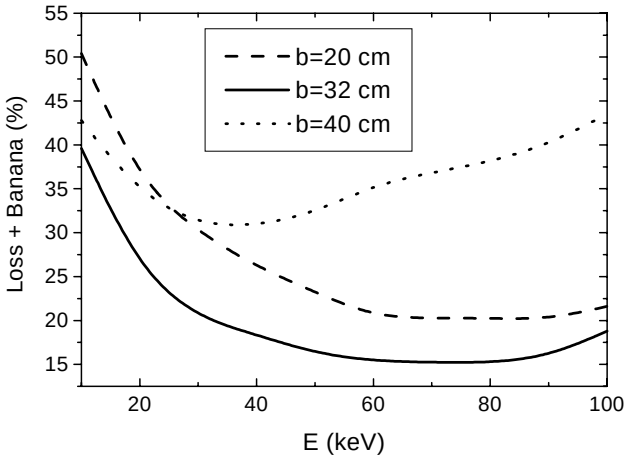

Figure 4. Spheromak, lost and trapped particles as a function of the injection energy.

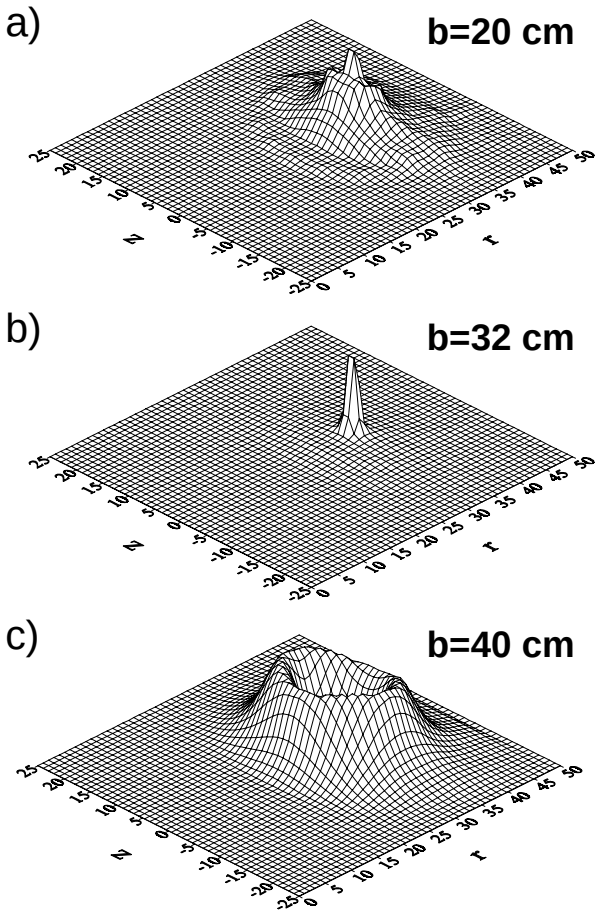

Figure 3. Spheromak, spatial distribution of beam ions after first orbit.

I.3 Current drive

Fig. 5 shows the beam plasma current as a function of the injection current (Fig. 5a) and energy (Fig. 5b) for FRCs with hollow ($D = 0.5$) and peaked ($D = -10$) profiles. At low injection current the beam current increases linearly. At higher currents, the deviation from a linear dependence is due to the increase in the local field and density produced by the beam current in the high β plasma. This effect is more noticeable for peaked equilibria. The dependence of the beam plasma current on the injection energy is complicated due to the variation of the ionization cross section and stopping power with energy. At high energy, the beam plasma current is significantly smaller for peaked equilibria due to the higher density produced by the effect discussed above.

In spheromaks, the beam plasma current shows a stronger dependence upon the impact parameter than in FRCs. This is seen in Fig. 6a which presents a plot of I_b as a function of b for $E_N = 20\ keV$ and $I_N = 100$ A. The maximum current is obtained when b is approximately equal to the radius of the magnetic axis (b_0). This is the result of a competition between two effects. When b is larger or smaller than b_0, the fraction of lost plus trapped particles increases as shown in Fig. 4. On the other hand, the density and stopping are larger at the magnetic axis. Fig. 6b shows that at low injection current ($I_N < 100A$) I_b increases almost linearly with I_N and that ,again, the maximum current is obtained when $b = b_0$. The dependence of I_b with the injection energy is shown in Fig. 6c for three values of the impact parameter. The case with $b = b_0$ shows again the highest beam plasma current.

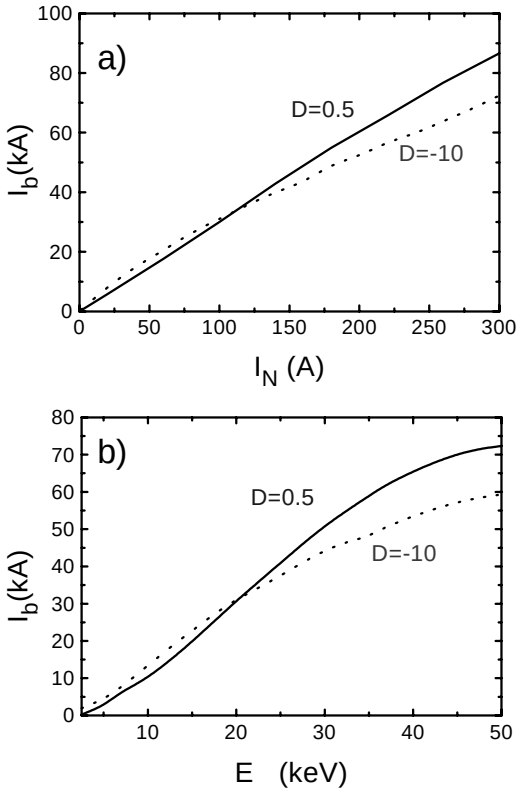

Figure 5. FRC, beam plasma current as a function on the injection current and energy.

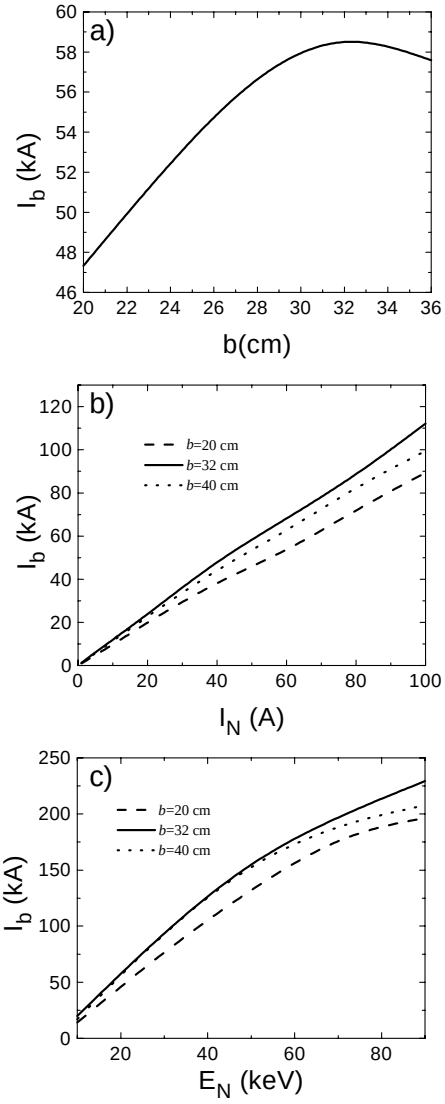

Figure 6. Spheromak, beam plasma current as a function of the impact parameter, injection current and injection energy.

Fig. 7 shows the spatial distributions of plasma and beam densities, beam current and transferred power for a peaked FRC equilibrium with $E_N = 20\ keV$, $b = 21cm$ and $I_N = 100\ A$. The peak in the plasma density is due to the effect of the beam current upon the equilibrium discussed above. The beam density shows two radial peaks which are due to fact that in their radial oscillations the particles spend more time at the turning points thus increasing the density in this region. A similar effect can be observed in the beam current distribution. The power transferred to the plasma does not show two peaks because it depends upon the values of the beam and plasma densities. In this case the peak in the plasma density is large enough to overcame the double peaked structure of the beam density. Fig. 8 shows similar plots for a spheromak with the same values of I_N and E_N and $b = 32\ cm$. It can be seen that the plasma density does not change appreciably due to the beam and that the beam current, density and power remain well localized around the magnetic axis.

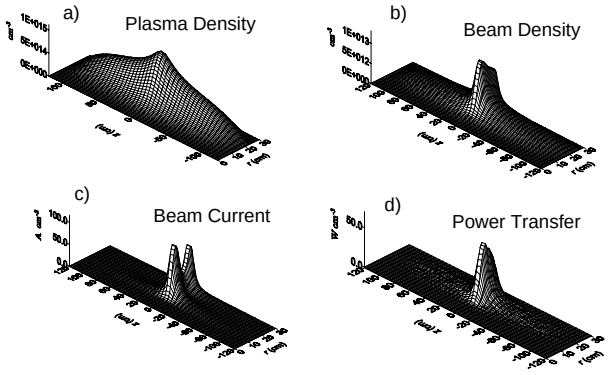

Figure 7. FRC, spatial distribution of plasma and beam densities, beam current and transferred power for $E_N = 20\ keV$, $b = 21\ cm$ and $I_N = 100A$.

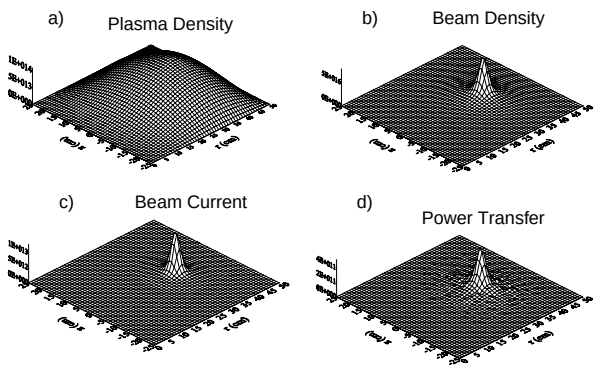

Figure 8. Spheromak, spatial distribution of plasma and beam densities, beam current and transferred power for $E_N = 20\ keV$, $b = 32\ cm$ and $I_N = 100A$.

II Rotating magnetic field current drive in spherical tokamaks

Rotating magnetic fields (RMF) have been used to drive current in Rotamaks [4] and FRC [5]. Although these devices generally operate without a stationary azimuthal (toroidal) magnetic field, some rotamak experiments included a conductor at the axis of the discharge vessel, producing configurations which are similar to spherical tokamaks (ST) [6]. Due to the current interest in STs, which has prompted the construction of several new devices, the development of RMF current drive as an efficient method for this concept would be of great importance.

II.1 Physical model and equations

The configuration considered is shown in Fig. 9. It consist of an infinitely long annular plasma column with inner radius r_a and outer radius r_b. Inside the column $r < r_a$ there is a uniform, stationary, axial current density that produces the *vacuum* toroidal field. The coils that produce the transverse, rotating magnetic field are assumed to be far from the plasma and their effect is introduced via the boundary conditions imposed at r_c ($r_c >> r_b$). The ions are considered to be fixed and the electrons are described using an Ohm's law that contains the Hall term:

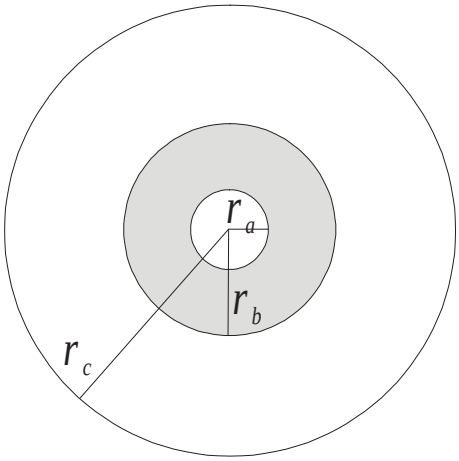

Figure 9. Cross section of the configuration employed.

$$\mathbf{E} = \eta \mathbf{j} + \frac{1}{en}\left(\mathbf{j} \times \mathbf{B}\right) \tag{3}$$

where η is the resistivity, which we assume to be uniform. Using Ohm's law and Maxwell's equations a set of coupled equations for B_z and A_z can be obtained. Since the contribution of the uniform axial current to A_z can be calculated analytically, we separate A_z in two parts: $A_z = A_{z,vac} + A_{z,pl}$, where $A_{z,vac}$ contains the contribution of the stationary axial current and $A_{z,pl}$ the contribution of the plasma and the external coils. Assuming that the rotating magnetic field produced by the coils can be written as:

$$\begin{aligned} B_r^{rot} &= -B_\omega \cos(\omega t - \theta) \\ B_\theta^{rot} &= -B_\omega \sin(\omega t - \theta) \end{aligned}$$

and normalizing the time with ω, the radius with r_b and the amplitude of the magnetic field with B_ω we obtain the following set of dimensionless equations:

$$\frac{\partial B}{\partial \tau} = \frac{1}{2\lambda^2}\left\{\nabla^2 B + \frac{\gamma}{\hat{r}}\left[\frac{\partial}{\partial \hat{r}}\left(\nabla^2 A\right)\frac{\partial A}{\partial \theta} - \frac{\partial}{\partial \theta}\left(\nabla^2 A\right)\left(\frac{\partial A}{\partial \hat{r}} - \frac{B_{tor}}{\hat{r}}\right)\right]\right\} \tag{4}$$

$$\frac{\partial A}{\partial \tau} = \frac{1}{2\lambda^2}\left\{\nabla^2 A + \frac{\gamma}{\hat{r}}\left[\left(\frac{\partial A}{\partial \hat{r}} - \frac{B_{tor}}{\hat{r}}\right)\frac{\partial B}{\partial \theta} - \frac{\partial A}{\partial \theta}\frac{\partial B}{\partial \hat{r}}\right]\right\} \tag{5}$$

where:

$$\hat{r} = \frac{r}{r_b}, \qquad \tau = \omega t, \qquad B = \frac{B_z}{B_\omega}, \qquad A = \frac{A_{z,pl}}{B_\omega\, r_b} \tag{6}$$

and B_{tor} is the vacuum toroidal field at $\hat{r} = 1$, normalized to B_ω. The two dimensionless parameters, γ and λ, are defined as:

$$\lambda = \frac{r_b}{\delta} = r_b \left(\frac{\mu_0 \omega}{2\eta}\right)^{1/2}, \qquad \gamma = \frac{\Omega_{\omega,e}}{\nu_{e,i}} = \frac{B_\omega}{en\eta}$$

where δ is the classical skin depth, $\Omega_{\omega,e}$ is the electron cyclotron frequency calculated with the amplitude of the RMF and $\nu_{e,i}$ is the electron-ion collision frequency ($\nu_{e,i} = \eta n e^2/m_e$). When $\gamma >> 1$, the electrons can be considered magnetized by the RMF. Knowing A and B, the other magnetic field components and the current density can be easily calculated.

II.2 Numerical method and boundary conditions

The computational domain is divided in three regions. In $0 \leq \hat{r} < \hat{r}_a$, region I, there is a uniform axial current and no plasma. Since A contains only the contribution of the plasma and the RMF we have: $\nabla^2 A = 0$. Since there are no azimuthal or radial currents in this region, B must be uniform (but can be time-dependent). Inside the plasma, $\hat{r}_a < \hat{r} < 1$, region II, we solve Eqs. 4 and 5. In $1 < \hat{r} < \hat{r}_c$, region III, there is vacuum and therefore B is uniform and $\nabla^2 A = 0$.

At $\hat{r} = \hat{r}_c$ we set:

$$A(\hat{r}_c) = \hat{r}_c \sin(\tau - \theta)\left(1 - e^{-\tau/\tau_0}\right), \tag{7}$$

where the exponential is introduced to allow for a slow "turn on" of the rotating field and $\hat{r}_c$ is taken large enough for the results to be independent of its specific value. At $\hat{r} = 1$ and $\hat{r} = \hat{r}_a$, the radial derivative of A must be continuous ($B_\theta = -\partial A_z/\partial r$). To obtain the results presented below, the value of B in region III was kept constant throughout the computation but it is also possible to introduce a flux conserver and adjust B after each time step to satisfy axial flux conservation. In region I, B is uniform but not constant (in time) and we calculate its value using Stoke's theorem. Considering a circumference of radius $\hat{r}_a + h$, where h is the radial grid spacing in region II, we can write:

$$B(I) \equiv B(\hat{r}_a) = \frac{1}{\pi \hat{r}_a^2}\left\{\int_0^{2\pi} A_\theta\left(\hat{r}_a + h, \theta\right)\hat{r}\, d\theta - \int_{\hat{r}_a}^{\hat{r}_a + h} d\hat{r}\,\hat{r} \int_0^{2\pi} d\theta\, B(\hat{r}, \theta)\right\} \tag{8}$$

The equation for the evolution of A_θ in region II is obtained from the θ-component of Ohm's law, using $\mathbf{E}$=-$\partial\mathbf{A}/\partial\mathbf{t}$.

II.3 Results

Normalized quantities are employed in the plots presented below and the efficiency is defined as the ratio between the azimuthal plasma current and the current that would be produced if all the electrons rotate rigidly with frequency ω. Fig. 10 is a plot of the steady-state efficiency vs. B_{tor} for $\gamma = 16.6$, $\lambda = 11.07$ and $r_a = 0.15$. The efficiency is 1, as in FRCs, when $B_{tor} = 0$ and decreases to 0.15 for $B_{tor} = 10$. It should be noted, however, that due to the larger radius of the plasma in a tokamak, as compared with an FRC, an efficiency of 0.15 could still result in a significant plasma current. Fig. 11 presents a similar plot for $\gamma = 14.9$ and the same values of λ and r_a as Fig. 10. In an FRC, the same values of λ and γ result in incomplete field penetration and an efficiency of 0.42 [7]. It can be seen in Fig. 11 that for small values of B_{tor} ($B_{tor} \lesssim 1.26$) there are two steady-state solutions. The initial conditions determine the branch towards which the system evolves. If we set $B_{tor} < B_{tor}^{crit}$ and start with a plasma column that has no azimuthal current, the steady-state solution follows the low efficiency branch (dashed line) in Fig. 11. When B_{tor} becomes larger than the critical value, and the same initial conditions are employed, the efficiency of the steady-state solution jumps to the full line in Fig. 11. To access the high efficiency solution for B_{tor} less than the critical value (dotted line) it is necessary to start with a steady-state solution having $B_{tor} > B_{tor}^{crit}$ and slowly decrease B_{tor}. The efficiencies obtained in the high efficiency branch of Fig. 11 ($\gamma = 14.9$), are very similar to the efficiencies obtained with $\gamma = 16.6$ (Fig. 10). This indicates that, in the presence of a steady toroidal field, plasmas having different values of γ can display a very similar behavior. In fact, the similarity between the high efficiency regime of Fig. 11 and the regime of Fig. 10 extends to the other features analyzed below (diamagnetism, current profile,

etc.). In what follows we will consider two regimes: the regime of Fig. 10, with $\gamma = 16.6$, and the low efficiency regime of Fig. 11, with $\gamma = 14.9$

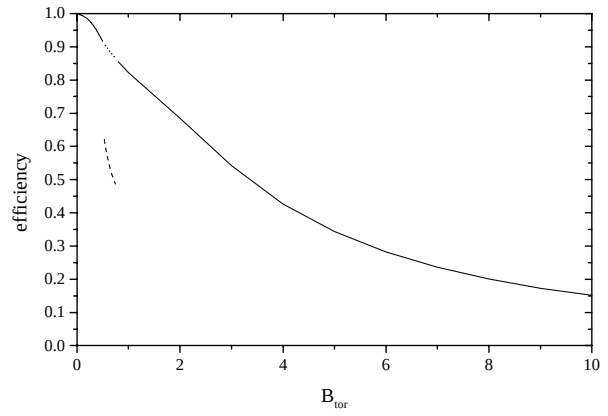

Figure 10. Efficiency vs. steady toroidal field for $\gamma = 16.6$, $\lambda = 11.07$ and $\hat{r}_a = 0.15$.

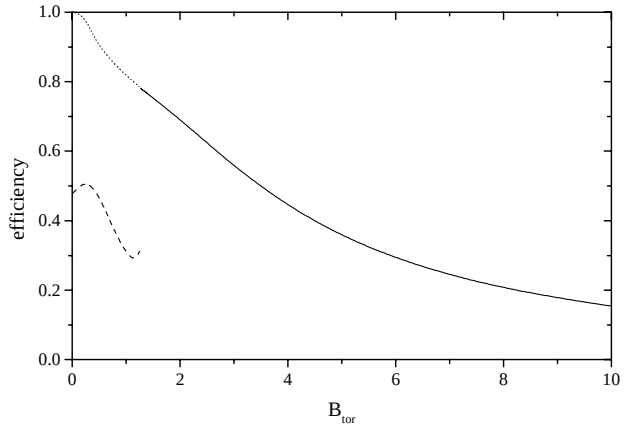

Figure 11. Efficiency vs. steady toroidal field for $\gamma = 14.9$, $\lambda = 11.07$ and $\hat{r}_a = 0.15$.

The effect of the steady toroidal field on the azimuthal current density profile is shown in Fig. 12, which presents a plot of the averaged (over θ) j_θ vs. r for the same parameters as Fig. 11 and three values of B_{tor}. When $B_{tor} = 0$ (full line) there is a large region, up to $r \cong 0.5$, inside the plasma with negligible current density and a narrow region, $r \geq 0.9$, on the outside where the electrons rotate rigidly with frequency ω. When $B_{tor} = 0.5$ (dashed line) the current density increases on the inside, in the region $0.3 \leq r \leq 0.5$, and decreases for $r \geq 0.6$, giving an overall increase in the total plasma current. Finally, when $B_{tor} = 1.15$, the current density is comparable to that obtained with B_{tor} =0 for $r \leq 0.6$ and significantly smaller at larger radius. The case with $\gamma = 16.6$ is shown in Fig. 13, which also presents a plot of $<j_\theta>$ vs. r for 3 values of B_{tor}. When $B_{tor} = 0$ the electrons rotate rigidly and the efficiency is 1. As the steady toroidal field increases, a region with negligible, even reversed, current density appears resulting in a reduction in the total current. As B_{tor} increases further the width of this region increases.

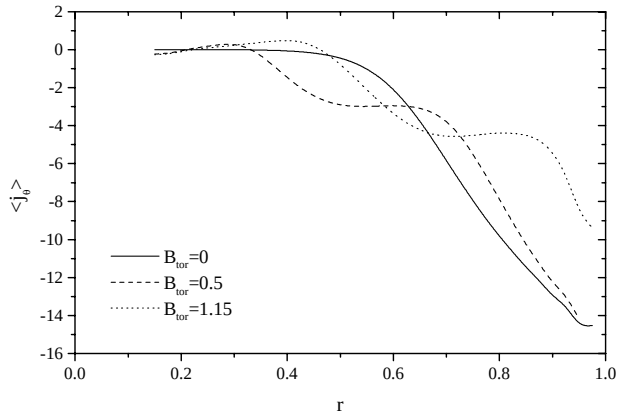

Figure 12. Averaged (over θ) azimuthal current density as a function of normalized radius for $\gamma = 14.9$, $\lambda = 11.07$, $\hat{r}_a = 0.15$ (low efficiency branch).

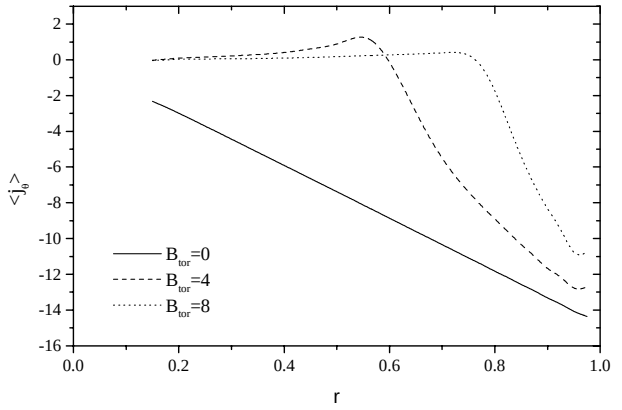

Figure 13. Averaged (over θ) azimuthal current density as a function of normalized radius for $\gamma = 16.6$, $\lambda = 11.07$, $\hat{r}_a = 0.15$ (high efficiency branch).

Experimental measurements and theoretical calculations in configurations with a steady toroidal field have shown the existence of poloidal currents, which are generally diamagnetic. We studied this issue for the two conditions indicated above. For the low efficiency regime of Fig. 11 there is a significant diamagnetic effect, which is shown in Fig. 14. This figure presents a plot of the ratio between the averaged (over θ) azimuthal field and the vacuum field as a function of r. For $B_{tor} = 0.5$ the diamagnetic well extends from $r \cong 0.3$ to the outer plasma boundary, with a maximum reduction in the total field of over 20% (compared with the vacuum value). For $B_{tor} = 1.15$ the width and depth of the well decrease but the diamagnetism continues to be significant. For the conditions of Fig. 10, $\gamma = 16.6$, the diamagnetism is negligible.

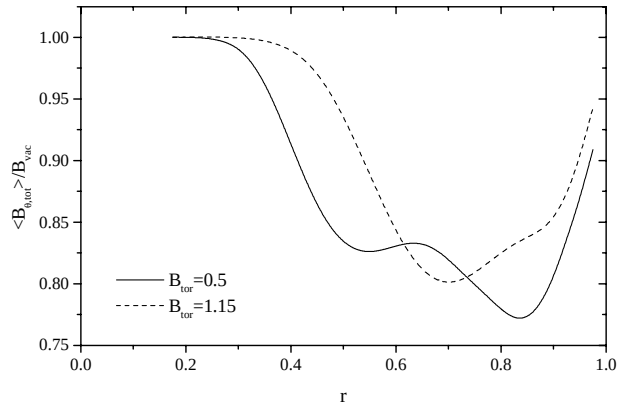

Figure 14. Ratio between the averaged, total, azimuthal field and the vacuum field for $\gamma = 14.9$, $\lambda = 11.07$ and $\hat{r}_a = 0.15$ (low efficiency branch).

II.4 Discussion

As a first step towards assessing the possibility of using RMF current drive in STs, we studied the effect of a steady toroidal field on this method. Our work presents two main improvements when compared to previous studies. The first is the use of a configuration which, albeit 2D, includes a hole at the center of the plasma thus providing a better representation of a tokamak. The second is the use of a fully 2D numerical code which solves the time dependent equations obtained from the basic physical model without further assumptions.

Although we did not attempt to make a detailed comparison with the experimental results of Ref. [6], it is clear that many of the qualitative features observed in these experiments are reproduced by the low efficiency branch of Fig. 2. Our results show that for some values of the external toroidal field, there are two steady-state solutions with different efficiencies. When the steady toroidal field is large compared to the rotating field, case of interest for STs, the efficiency is small but the total current could still be significant if operation at frequencies of the order of 10^6 Hz is possible. Further studies should be done to find the best operating regime for STs and the corresponding efficiency and required power. In addition, improved physical models should be developed to remove some of the most critical assumptions employed in this study. A step in this direction has been recently done by Milroy [8] who employed an MHD model to study RMF current drive in FRCs.

III Minimum dissipation states for flux core spheromaks sustained by helicity injection

The use of helicity injection to sustain a spheromak is very attractive because of its simplicity and high efficiency. In general, helicity injection current drive is explained by assuming that the plasma undergoes some form of relaxation that allows for a redistribution of the magnetic flux. In this context, *relaxation principles* provide a relatively simple method to predict the final state of plasmas driven by helicity injection. Taylor and Turner [9] applied the well known minimum energy principle to a flux core spheromak sustained by helicity injection through the polar caps. Although this principle has been successful at explaining the reversal of the magnetic field in the RFP, its use in driven systems remains questionable. In such systems, other principles that allow for the introduction of balance constraints (injection rate=dissipation rate) could be more appropriate. One such principle, the principle of minimum rate of energy dissipation, has been already used to calculate the relaxed states of tokamaks sustained by helicity injection [10] [11].

In this paper we employ the principle of minimum rate of energy dissipation to calculate relaxed states of a flux core spheromak sustained by helicity injection. Although the geometry considered is very simple, the result could be of interest for the recently proposed PROTO-SPHERA experiment [12].

III.1 Minimization, Euler-Lagrange equations

We assume that the plasma is stationary ($\mathbf{v} = \mathbf{0}$) and minimize the Ohmic dissipation rate subject to the constraints of helicity balance (injection rate=dissipation rate) and $\nabla \cdot \mathbf{B} = \mathbf{0}$. This is done by introducing the following functional:

$$W = \int \eta j^2 \, dV - \frac{\lambda}{\mu_0} \left[\int \eta \mathbf{j} \cdot \mathbf{B} \, \mathbf{dV} + \oint \varphi \mathbf{B} \cdot \mathbf{dS} \right] - \gamma \int \nabla \cdot \mathbf{B} dV \tag{9}$$

where η is the plasma resistivity, φ is the applied electrostatic potential and λ and γ are Lagrange multipliers. In eq.(9), the first three terms in the RHS are, respectively, the Ohmic dissipation rate, the helicity dissipation rate and the helicity injection rate. Setting the first variation of W equal to zero the cancellation of the volume term gives the following Euler-Lagrange equation:

$$\nabla \times \mathbf{j} - \lambda \mathbf{j} + \frac{\mu_0}{2\eta} \nabla \gamma = 0 \qquad (10)$$

the boundary conditions needed to solve this equation are obtained from the physical situation considered (flux core spheromak sustained by helicity injection through the polar caps) and from the cancellation of the surface term in δW.

III.2 Results

Equation (10) is solved numerically using cylindrical coordinates ($\partial/\partial\theta \equiv 0$) for the configuration shown in Fig. 15, which consists in a cylindrical flux conserver with radius equal to its height (0.4 m) and two electrodes. The radius of the electrodes is one fifth of the radius of the flux conserver and it is assumed, for simplicity, that the magnetic field on the electrodes is uniform and is an externally controlable parameter. In reality, the flux passing through the electrodes depends on the current flowing in the external coils (not shown) and the plasma current. Our assumption is that the current in the external coils is adjusted until the desired field on the electrodes is obtained.

The method of solution consists in guessing a value for λ and solving the Euler-Lagrange equations. Using the calculated current and magnetic field profiles, the helicity injection and dissipation rates are calculated and compared. If they agree the value of λ is accepted, if not a new value is chosen and the procedure repeated. Fig. 16 shows flux contours obtained for $V_e/B_z = 10^3 V/T$. The solution in Fig. 16 a has $\lambda = 12.2157\ m^{-1}$ and an energy dissipation rate (W_{dis}) of $1.56\ 10^{12}\ W$ while the solution in Fig. 16 b has $\lambda = 12.2223\ m^{-1}$ and W_{dis}=$1.60\ 10^{12}\ W$. It is clear that altough both are solutions of the Euler-Lagrange equations (both are extrema of the functional), the solution that minimizes the dissipation rate is the one in Fig. 16 a. For $12.2157\ m^{-1} < \lambda < 12.2223\ m^{-1}$ solutions with almost no open flux are obtained but they do not satisfy the helicity balance constraint.

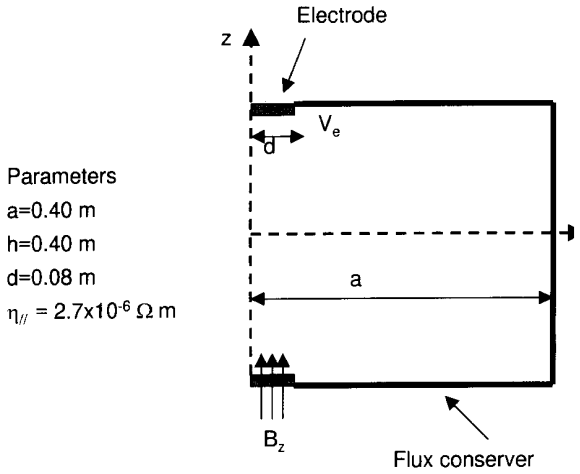

Figure 15. Configuration employed for the flux core spheromak.

Fig. 17 shows a sequence of solutions obtained for decreasing values of V_e/B_z. It is clear that decreasing V_e/B_z reduces the size of the closed flux region. The behavior of the Lagrange multipliers corresponding to the solutions with high and low dissipation is shown in Fig. 18, which presents a plot of λ as a function of $\log(V_e/B_z)$. It is seen that both values are very close and that the difference between them decreases when V_e/B_z decreases. In fact, both values of λ are close to the eigenvalue of the equation $\nabla \times \mathbf{j} = \lambda \mathbf{j}$ with $\mathbf{j}.\hat{\mathbf{n}} = \mathbf{0}$ at the boundary for elongation equal to 1 [13]. Fig. 19 presents a plot of the total plasma current (on open and closed surfaces) as a function of the applied voltage for $B_z = 0.1\,T$. This figure shows that significant currents can be obtained for reasonable values of applied voltage and magnetic field. Of course, this will depend on the value of the resistivity, which was assumed to be $2.7 \times 10^{-6}\ \Omega m$ in this calculation. To conclude, we present in Fig. 20 2D plots of the toroidal magnetic field and the toroidal current density for the minimum dissipation solution with $V_e = 1000V$ and $B_z = 1\,T$ (see Fig. 16). This shows that if a large enough magnetic field can be produced large currents could result at relatively low voltages.

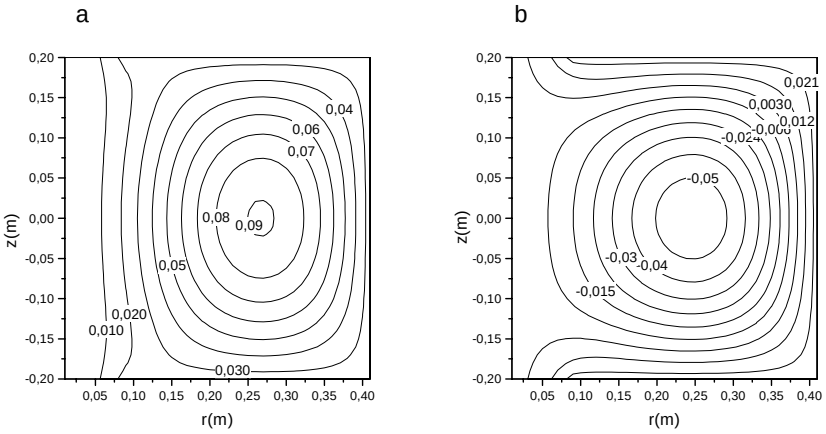

Figure 16. Flux surfaces for the two solutions with $V_e/B_z = 10^3\, V/T$.

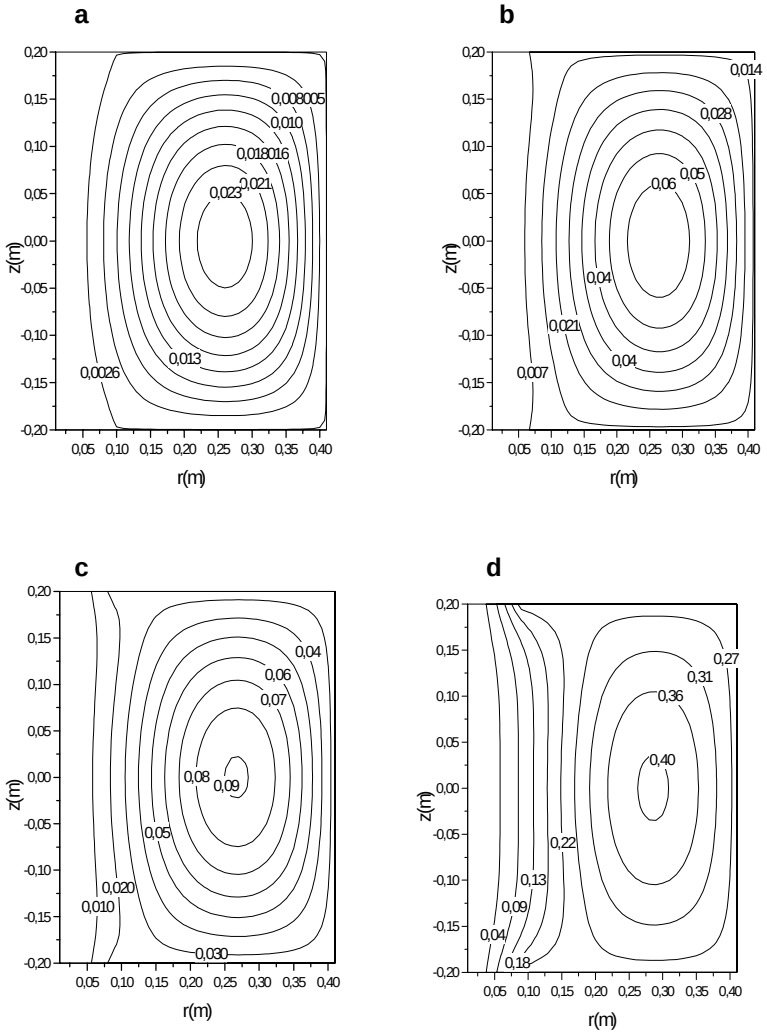

Figure 17. Flux surfaces of the solutions obtained for various values of V_e/B_z.

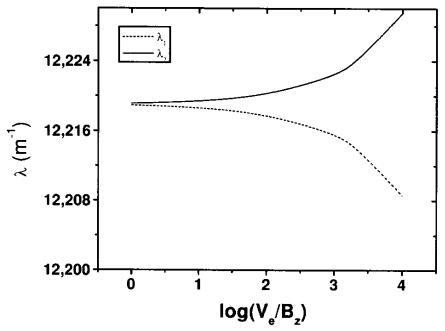

Figure 18. Value of the Lagrange multiplier as a function of $\log(V_e/B_z)$.

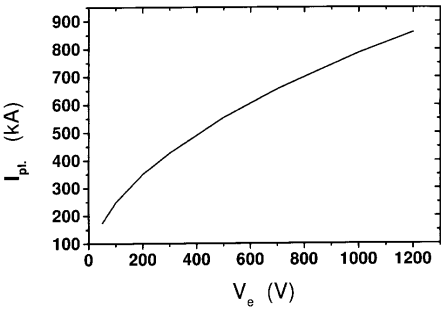

Figure 19. Plasma current as a function of applied voltage for $B_z = 0.1T$.

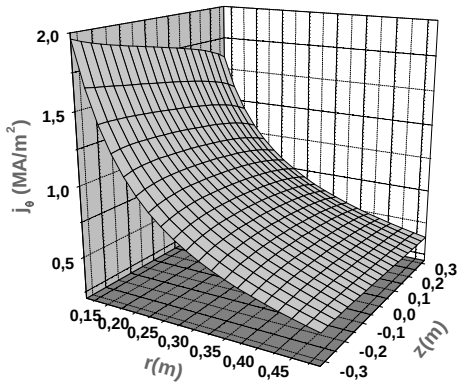

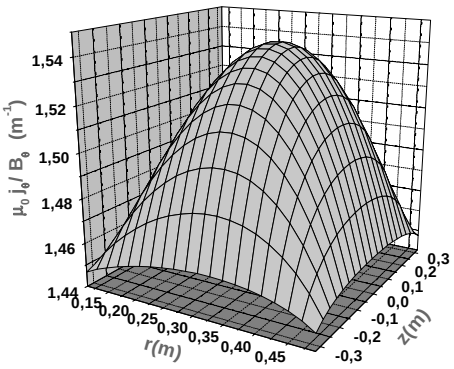

Figure 20. 2D plots of the toroidal magnetic field and current density for $V_e = 1000\ V$ and $B_z = 1T$.

III.3 Discussion

We have shown that the relaxed states of a flux core spheromak calculated using the minimum dissipation principle have closed flux surfaces and significant plasma current. Although there are solutions of the Euler-Lagrange equations which satisfy the helicity balance constraint and have the open flux region on the outside, they have higher dissipation rates than those with the open flux on the inside and therefore can not be considered as true solutions of the minimization problem. The Lagrange multipliers of both solutions are very close and their value is approximately equal to the inverse of the electrode radius. Future work on this problem should include the use of anisotropic/non-uniform resistivity.

Acknowledgements

This work was partially supported by grants from the International Atomic Energy Agency (contract N 10527/RI) and the Agencia Nacional de Promocion Cientifica y Tecnologica of Argentina (PICT 99). One of the authors (RAC) would like to thank the Conselho Nacional de Desenvolvimento Cientifico y Tecnologico (CNPq), Brazil, for financial support.

References

[1] H. Momota, Fusion Technol **21**, 2307 (1992).

[2] Phys. Plasmas **7**, 2294 (2000)

[3] R. Bartiromo, Phys. of Plasmas **6**, 1830-1836 (1999).

[4] I. R. Jones, Phys. Plasmas **6**, 1950 (1998).

[5] J. T. Slough and K. E. Miller, Phys. Rev. Lett. **85**, 1444 (2000).

[6] G. A. Collins, G. Durance, G. R. Hogg, J. Tendys, P. A. Watterson, Nucl. Fusion **28**, 255 (1988).

[7] R. D. Milroy, Phys. of Plasmas **6**, 2771 (1999).

[8] R. D. Milroy, Phys Plasmas **7**, 4135 (2000).

[9] J. B. Taylor and M. F. Turner, Nucl. Fusion **29**, 219 (1989).

[10] R. Farengo y J. R. Sobehart. Plasma Phys. Control. Fusion **36**, 1691 (1994).

[11] K. I. Caputi and R. Farengo, Plasma Phys. and Contr. Fusion **43**, 795-804 (2001).

[12] F. Alladio, private communication (1999).

[13] J. M. Finn, W. M. Manheimer and E. Ott, Phys. Fluids **24**, 1336 (1981).